ORIGINAL ARTICLE

Numerical simulation of particle-driven gravity currents

Sangdo An · Pierre Y. Julien ·
Subhas K. Venayagamoorthy

Abstract Particle-driven gravity currents frequently occur in nature, for instance as turbidity currents in reservoirs. They are produced by the buoyant forces between fluids of different density and can introduce sediments and pollutants into water bodies. In this study, the propagation dynamics of gravity currents is investigated using the FLOW-3D computational fluid dynamics code. The performance of the numerical model using two different turbulence closure schemes namely the renormalization group (RNG) k–ϵ scheme in a Reynold-averaged Navier-Stokes framework (RANS) and the large-eddy simulation (LES) technique using the Smagorinsky scheme, were compared with laboratory experiments. The numerical simulations focus on two different types of density flows from laboratory experiments namely: Intrusive Gravity Currents (IGC) and Particle-Driven Gravity Currents (PDGC). The simulated evolution profiles and propagation speeds are compared with laboratory experiments and analytical solutions. The numerical model shows good quantitative agreement for predicting the temporal and spatial evolution of intrusive gravity currents. In particular, the simulated propagation speeds are in excellent agreement with experimental results. The simulation results do not show any considerable discrepancies between RNG k–ϵ and LES closure schemes. The FLOW-3D model coupled with a particle dynamics algorithm successfully captured the decreasing propagation speeds of PDGC due to settling of sediment particles. The simulation results show that the ratio of transported to initial concentration C_o/C_i by the gravity current varies as a function of the particle diameter d_s. We classify the transport pattern by PDGC into three regimes: (1) a suspended regime (d_s is less than about 16 µm) where the effect of particle deposition rate on the propagation dynamics of gravity currents is negligible i.e. such flows behave like homogeneous fluids (IGC); (2) a mixed regime (16

S. An (✉) · P. Y. Julien · S. K. Venayagamoorthy
Department of Civil and Environmental Engineering, Colorado State University, Fort Collins,
CO 80523-1372, USA
e-mail: sdan99@engr.colostate.edu

P. Y. Julien
e-mail: pierre@engr.colostate.edu

S. K. Venayagamoorthy
e-mail: vskaran@engr.colostate.edu

μm $< d_s <$ 40 μm) where deposition rates significantly change the flow dynamics; and (3) a deposition regime ($d_s >$ 40 μm) where the PDGC rapidly loses its forward momentum due to fast deposition. The present work highlights the potential of the RANS simulation technique using the RNG k–ϵ turbulence closure scheme for field scale investigation of particle-driven gravity currents.

Keywords Gravity currents · Density currents · Buoyant forces · Computational fluid dynamics (CFD) · Lock-exchange flows · Particle settling · Environmental fluid mechanics

1 Introduction

Many kinds of gravity currents, produced by the density difference between different fluids, are observed in nature. They are also known as "density currents" or "buoyancy-driven currents". The density differences generally arise due to temperature variations, dissolved material or suspended solids [37,41]. Thus, the formation and evolution of gravity currents are influenced by various natural conditions. In water environments, saline intrusions or oil spills in the oceans, turbid water intrusions in a lake, and suspended sediment plumes in a river are good examples. They frequently introduce harmful pollutants into the water bodies [8], and thus an understanding of their dynamics and prediction of their fate are crucial for managing water quality.

The field investigation of gravity currents is usually very difficult due to their complicated and unexpected occurrence characteristic. On the other hand, scaled laboratory experiments have been widely used to elucidate the dynamics of gravity currents. Many studies have investigated various aspects of gravity currents using lock-exchange experiments. In some of the earlier experiments, gravity currents were commonly generated by releasing dense fluid ρ_d into uniform ambient fluid ρ_a [17,24,28,36]. In such a case, the gravity current will propagate along the bottom surface and is referred to as a Bottom Boundary Gravity Current (hereafter called BBGC, see Fig. 1). Benjamin [3] suggested that for energy-conserving flows, $U_d = 0.5\sqrt{g'H}$ where U_d is the propagation speed of a gravity current, $g' = g(\rho_d - \rho_a)/\rho_a$ is the reduced gravity, and H is the total water depth in a tank. The experiments of Keulegan [24] determined that the equation for initial velocity was given by $U_d = 0.462\sqrt{g'H}$. Von Kármán [43] derived a theoretical formula for the propagation speed of a BBGC based on the Bernoulli equation assuming an ideal fluid and irrotational flow. This is given by $U_d = 1.41\sqrt{g'h_d}$, where h_d is the height of a gravity current.

When there is an ambient two-layered fluid system and the density of the lock fluid is equal to the average of the densities of the two ambient fluids (see Fig. 2), the gravity current will propagate along the interface between the upper and the lower fluid layers and is commonly referred to an Intrusive Gravity Current (hereafter called IGC). The dynamics of IGC propagating into a two-layer fluid was investigated experimentally [4,11,22,34,39].

Fig. 1 Sketch of lock-exchange experiment for a bottom boundary gravity current (*BBGC*)
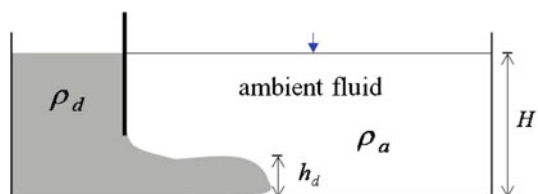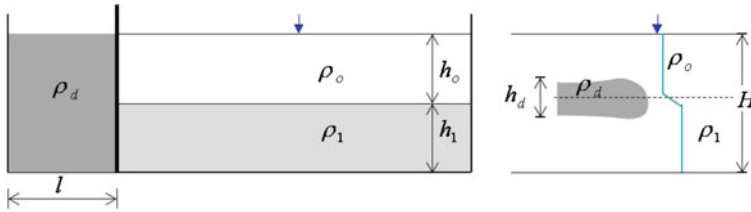
Fig. 2 Sketch of lock-exchange experiment for an intrusive gravity current (*IGC*)

Lowe et al. [26] derived analytical solutions for propagation speeds based on the analysis of Holyer and Huppert [22] and Rooij et al. [34]. They applied Bernoulli's principle along streamlines assuming the flow to be energy-conserving. For the energy-conserving gravity current with a small density difference between the upper and lower fluids and with $\rho_d = (\rho_o + \rho_1)/2$, they determined that $U_d = 0.5\sqrt{g'_o H/2}$, where $g'_o = 0.5g(\rho_1 - \rho_o)/\rho_o$. For defining more complicated types of flow in a two-layer fluid, three dimensionless parameters (ϵ, σ, Δ) were introduced in Sutherland et al. [39]. The dimensionless parameter ϵ is defined as the relative density difference between the gravity current and ambient fluid layers, given by $\epsilon = (\rho_d - \bar{\rho})/(\rho_1 - \rho_o)$. Here, the depth-weighted average density is $\bar{\rho} = (\rho_o h_o + \rho_1 h_1)/H$ and ρ_d is the density of fluid in the lock. Therefore, the experiments with $\epsilon = 0$ correspond to cases in which the density of the lock fluid is equal to the depth-weighted average density of the upper and lower layers ($\rho_d = \bar{\rho}$). Another parameter σ is used to characterize the relative density difference between the upper and lower layers, defined as $\sigma = (\rho_1 - \rho_o)/\rho_o$. The relative depth of the upper and lower layer ambient fluids compared with the total depth is characterized with the parameter $\Delta = (h_o - h_1)/H$. For example, experiments with $\Delta = 0$ correspond to cases in which the upper and lower layers have equal depth. Holyer and Huppert [22] extended the theory derived by Benjamin [3] to describe the dynamics of interfacial gravity currents. Sutherland et al. [39] adapted the theory of Holyer and Huppert [22] to develop an empirical prediction for propagation speed. They defined the symmetric degree of intrusion into a two-layer fluid using ϵ and Δ. When the fluid density contained behind the lock gate is equal to the depth-weighted average densities of the ambient two layer fluid, the intrusive gravity current is regarded as a symmetrical flow, $\epsilon = 0$. A more symmetrical intrusive gravity current occurs when both ϵ and $\Delta = 0$, while asymmetrical cases occur when $\epsilon \neq 0$. For ϵ and $\Delta = 0$, the equation for the propagation speed can be simplified to $U_d/\sqrt{g\sigma H} \simeq 0.25$. This is identical to the formula of Lowe et al. [26]. For the symmetrical cases, the experiments of Sutherland et al. [39] showed excellent agreement with theoretical analysis while highlighting that the role of interfacial waves were negligible (i.e. the interface in front of the intrusion remains stable and undisturbed).

In the last decade, Computational Fluid Dynamics (CFD) has increasingly been used to investigate gravity currents and has resulted in better understanding of their dynamics. Härtel et al. [18] investigated lock-exchange flows in an infinite channel using Direct Numerical Simulations (DNS). Their simulations successfully reproduced the formation of the lobe and cleft instability that occurs at the head of a gravity current. Fringer et al. [13] presented numerical results of lock-exchange gravity currents using the SUNTANS model and discussed the difference between hydrostatic and non-hydrostatic simulation results. They showed that the hydrostatic simulation can not capture the formation of the Kelvin–Helmholtz billows and does not reproduce the propagation speed correctly. In contrast the non-hydrostatic simulation captured both the propagation speed and the Kelvin–Helmholtz billows correctly. Ooi et al. [30] studied qualitative and quantitative aspects of the dynamics of gravity currents

using Large Eddy Simulation (LES). Their model was validated using the results of Härtel et al. [18] and showed very good agreement of propagation speeds. In nature, gravity currents can be produced by an increased bulk density due to suspended particles. In particular, during a severe flood event, gravity currents in rivers or lakes are usually induced by high suspended sediment loads from watersheds, and are known as "Particle-Driven Gravity Currents (PDGC) or turbidity currents". PDGC are very important in many environmental flows due to their influence on water quality [2]. Turner [40] theoretically derived the governing equations for slowly varying gravity currents on a slope. These governing equations were modified by Parker et al. [31] in order to add the effects of resuspension from the erodible bed. They proposed an empirical relation, coupled with a simplified integral model to compute the erosion and deposition of the bottom boundary during passage of PDGC. Altinakar et al. [1] carried out laboratory experiments with various slopes and particle diameters. They found that the deposition rate of sediments is related to the propagation speed and the thickness of PDGC. However, the application of such theoretical approaches and/or integral models to PDGC requires empirical data from extensive laboratory experiments for verification and validation.

In this regard, numerical models are attractive, since once validated, they can be used to perform parametric studies in order to gain insights on the dynamics of PDGC. However, numerical prediction of PDGC is more complex than that of homogeneous gravity currents because the buoyancy flux of PDGC varies both temporally and spatially depending on how particles move in turbulent flows (due to advection, settling and resuspension). This makes CFD simulations of PDGC quite challenging and interesting [5,7,23,42]. Necker et al. [29] presented high-resolution simulations of density currents and extended their work to include resuspending PDGC. De Cesare et al. [9] used a 3-D numerical model to account for the sediment transport and deposition in a reservoir by PDGC to study volume reduction in reservoirs. Chung et al. [8] employed the Estuary Lake and Coastal Ocean Model (ELCOM) for simulations of hydrodynamic processes, coupled with the Computational Aquatic Ecosystem DYnamics Model (CAEDYM) to simulate the particle dynamics. Heimsund [19] evaluated the usefulness of FLOW-3D in order to simulate turbidity currents on deep-sea floors and found good agreement between simulation and laboratory experimental results. Georgoulas et al. [14] presented 3-D simulations of turbidity currents using the commercial code FLUENT using the RNG k–ϵ turbulence model [44]. They employed a multi-phase numerical approach which provides separate velocity fields for each phase (water phase and sediment phase). De Cesare et al. [10] used CFX-4 model coupled with an erosion-deposition model to evaluate the impact of turbidity currents on water quality of Lake Lugano.

The objective of the present study is to explore the dynamics of IGC and PDGC using the 3-D non-hydrostatic FLOW-3D CFD code [12] and hence demonstrate the applicability of the code for studying PDGC at the field scale. We are able to simulate IGC and PDGC consisting of different particle sizes by incorporating a particle dynamics algorithm into the code. The ability of the numerical model to predict various important dynamics of IGC and PDGC such as propagation speed, intrusion height and thickness, and the effect of particle sizes on propagation speed is justified by comparing numerical results with laboratory experiments in literature [16,39]. In Sect. 2, we provide a brief description for the computational approach we employ for this study. An overview of the problem set-up and a summary of all the simulation cases are described in Sect. 3. We then present and discuss simulation results in Sect. 4. In the first part of the Sect. 4, we present the results and analysis of IGC simulations. In the second part of the Sect. 4, we present novel results from a series of numerical simulations of PDGC to highlight the effects of different particle settling rates on propagation speeds. The numerical predictions are compared with lock-exchange experiments [16], as shown in Fig. 3. We finally draw some conclusions in Sect. 5.
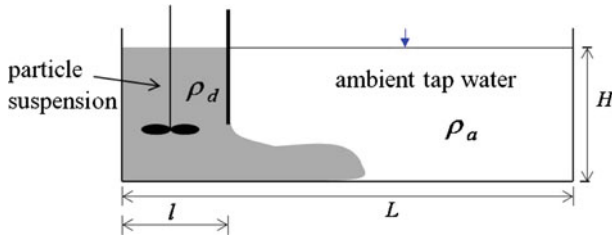
Fig. 3 Sketch of lock-exchange experiment for a particle-driven gravity current (*PDGC*)

2 Numerical methodology

2.1 Overview of FLOW-3D code

We employ the FLOW-3D CFD code to both examine how well the model captures the dynamics of gravity currents as well gain insights on PDGC. FLOW-3D is a commercial code capable of fluid-boundary tracking and resolves fluid-fluid and fluid-air interfaces using highly-resolved structured meshes. The model provides transient, 3-D numerical solutions to multi-scale, multi-physics flow problems. It is ideally suited for free-surface flows since it exploits the highly accurate improved Volume of Fluid (VOF) technique [21] to predict the free surface. In addition to the VOF technique, the structured FAVOR(Fractional Area-Volume Obstacle Representation) method [20] is used to get accurate geometric representations of complex geometries in the computational domain that is based on rectangular volume cells. The FAVOR method is also employed to eliminate flow losses, which may result from using a Cartesian grid system. In general, a Cartesian grid representation of a curved flow regime can result in considerable numerical flow losses due to a zigzag approximation for the interface between flow and obstacles. The FAVOR technique eliminates the zigzag directional changes by smoothly blocking out fractional portions of grid cell faces and volumes. The model numerically solves the fluid flow governing equations using the finite-volume approach. In the FAVOR technique, all variables are stored at cell centers except for velocities which are recorded at cell-faces.

2.2 Governing equations

The model simultaneously solves the 3-D Reynolds-averaged Navier-Stokes (RANS) equations for fluid flow with the Boussinesq approximation, the conservation of mass equation, and scalar transport equations. The governing equations are coupled with the equations of state relating density to temperature, sediment concentration, and sediment particle settling. A scalar transport equation can be used to compute advection, diffusion, and dispersion of scalars (e.g. sediment concentration and temperature). These equations are given in tensor notation by

$$\frac{\partial u_i}{\partial t} + u_j \frac{\partial u_i}{\partial x_j} = -\frac{1}{\rho_r} \frac{\partial p}{\partial x_i} + \frac{\partial}{\partial x_j} \left(v \frac{\partial u_i}{\partial x_j} - \overline{u_i' u_j'} \right) + g_i \frac{\rho - \rho_r}{\rho_r}, \tag{1}$$

$$\frac{\partial u_i}{\partial x_i} = 0, \tag{2}$$

$$\frac{\partial \phi}{\partial t} + \frac{\partial}{\partial x_i} (u_i \phi) = \frac{\partial}{\partial x_i} \left(\Gamma \frac{\partial \phi}{\partial x_i} - \overline{u_i' \phi'} \right), \tag{3}$$

where u_i are the mean velocity components in a Cartesian coordinate system (x, y, z); t is time; ρ_r is the reference density; p is the total pressure; ν is the fluid kinematic viscosity; $-\overline{u'_i u'_j}$ are Reynolds stresses; g is the gravitational acceleration; ϕ is the mean scalar; Γ is the molecular diffusivity of the scalar ϕ; $-\overline{u'_i \phi'}$ is the turbulent fluxes of the scalar ϕ; and ρ is density which can be calculated as a function of temperature and concentration. The overbar (-) implies averaging of fluctuating quantities. Equation (3) is a scalar transport equation which can be used to solve for the scalar field (e.g. sediment concentration or temperature etc.) and it is coupled with Eq. (1) only through the buoyancy term with the Boussinesq approximation.

2.3 Turbulence modeling

Most flows of engineering interest are turbulent which precludes direct numerical solutions due to prohibitively costly simulations. Hence, RANS simulations are commonly used to obtain mean flow quantities for engineering applications. However, the RANS formulation results in additional terms $\overline{u'_i u'_j}$ and $\overline{u'_i \phi'}$ in Eq. (1) and (3), respectively. The $\overline{u'_i u'_j}$ term represents momentum fluxes induced by the turbulence and can be viewed as additional stress terms (the so-called Reynolds stresses) that need to be modeled (an in-depth discussion on turbulence modeling is given in [32]). A common approach to model the Reynolds stresses is to use the turbulent viscosity hypothesis due to Boussinesq (see [32,35]):

$$-\overline{u'_i u'_j} = \nu_t \left(\frac{\partial u_i}{\partial x_j} + \frac{\partial u_j}{\partial x_i} \right) - \frac{2}{3} k \delta_{ij}, \tag{4}$$

where ν_t is the turbulent (eddy) viscosity, δ_{ij} is the Kronecker delta, k is the turbulent kinetic energy. The $\overline{u_i \phi}$ term in Eq. (3) represents the turbulent scalar flux and is given by

$$-\overline{u'_i \phi'} = \Gamma_t \frac{\partial \phi}{\partial x_i}, \tag{5}$$

where Γ_t is a turbulent scalar diffusivity defined as $\Gamma_t = \nu_t / Sc_t$ where Sc_t is the turbulent Schmidt number, generally determined by laboratory experiments.

In order to close the system of mean flow equations (Eqs. (1) and (3)), a turbulence model is required. The most common turbulence models in engineering flow analysis are the so called two-equation eddy viscosity models (e.g. k–ϵ model). The FLOW-3D code provides several turbulence closure schemes, including the standard k–ϵ model, the renormalization-group (RNG) k–ϵ model, and the large-eddy simulation (LES) technique. In this study, we use the RNG k–ϵ within the RANS framework and the LES technique. In the RNG k–ϵ model, the eddy viscosity is given by

$$\nu_t = c_\mu k^2 / \epsilon. \tag{6}$$

In Eq. (6), the turbulent kinetic energy k and its dissipation rate ϵ are obtained from the following transport equations.

$$\frac{\partial k}{\partial t} + u_j \frac{\partial k}{\partial x_j} = \frac{\partial}{\partial x_j} \left(\frac{\nu_t}{\sigma_k} \frac{\partial k}{\partial x_j} \right) + P + G - \epsilon, \tag{7}$$

$$\frac{\partial \epsilon}{\partial t} + u_j \frac{\partial \epsilon}{\partial x_j} = \frac{\partial}{\partial x_j} \left(\frac{\nu_t}{\sigma_\epsilon} \frac{\partial \epsilon}{\partial x_j} \right) + c_{1\epsilon} \frac{\epsilon}{k} (P + c_{3\epsilon} G) - c_{2\epsilon} \frac{\epsilon^2}{k} - R_\epsilon, \tag{8}$$

where P, G, and R are defined as

$$P = \nu_t \left(\frac{\partial u_i}{\partial x_j} + \frac{\partial u_j}{\partial x_i} \right) \frac{\partial u_i}{\partial x_j}, \tag{9}$$

$$G = \frac{g_i}{\rho_r} \frac{\nu_t}{Sc_t} \frac{\partial \rho}{\partial x_i}, \tag{10}$$

$$R_\epsilon = \frac{c_\mu \eta^3 (1 - \eta/\eta_o)}{1 + \beta \eta^3} \frac{\epsilon^2}{k}, \tag{11}$$

where c_μ=0.085; $c_{1\epsilon}$=1.42; $c_{2\epsilon}$=1.83; $c_{3\epsilon}$=0.2; σ_k=1.39; σ_ϵ=1.39; β=0.015; and η_o=4.38 [11,43]. The parameter η is the ratio of the turbulent time scale (k/ϵ) to the mean strain time scale S), given by

$$\eta = S \frac{k}{\epsilon}, \tag{12}$$

where $S = \sqrt{2 S_{ij} S_{ij}}$ and S_{ij} represents the strain rate tensor given by

$$S_{ij} = \frac{1}{2} \left(\frac{\partial u_i}{\partial x_j} + \frac{\partial u_j}{\partial x_i} \right). \tag{13}$$

In addition to the RANS simulations, this study presents LES simulations that provide more detailed information about interfacial turbulence between a gravity current and the ambient fluid. In the LES technique, large eddies are resolved directly, but small eddies are modeled using a subgrid-scale turbulence model. For the large eddies, the governing equations are obtained by filtering them in either Fourier space (wave-number) or physical space. The subgrid-scale turbulence model adopted in the model is based on the turbulent viscosity hypothesis analogous to the RANS approach (for details, please see [25,32]). In the subgrid model, the Reynolds stresses are defined as follows:

$$\tau_{ij} = 2 \frac{\mu_t}{\rho} S_{ij} - \frac{2}{3} \rho k \delta_{ij}, \tag{14}$$

where μ_t denotes the subgrid-scale turbulent dynamic viscosity. Smagorinsky [38] defined μ_t as

$$\mu_t = \rho (cL)^2 \sqrt{S_{ij} S_{ij}}, \tag{15}$$

where c is a constant (usually taken to be about 0.2) and L is a length scale defined as the geometric mean of the grid cell dimensions given by

$$L = (\delta x \delta y \delta z)^{1/3}. \tag{16}$$

2.4 Coupling a particle dynamics model with FLOW-3D

General flow situations are approximated using incompressible fluids for engineering applications, but in some situations, it is important to include the effect of buoyant forces associated with small density variations. The Flow-3D model provides a solution of the flow, influenced by buoyant forces, by coupling its incompressible flow solution algorithm with an energy transport equation and a local evaluation of the density as a function of temperature. We developed a new particle algorithm which is coupled with the FLOW-3D to simulate the effect of different particle deposition rates. In the particle dynamic model, the settling velocities ω_s are computed as a function of each particle's diameter d_s and corresponding density ρ_s according to Stokes' law.

Fig. 4 Schematic of the
concentration change due to
particle deposition in cell
(i, j, k). C_{ijk} indicates the
concentration in cell (i, j, k)
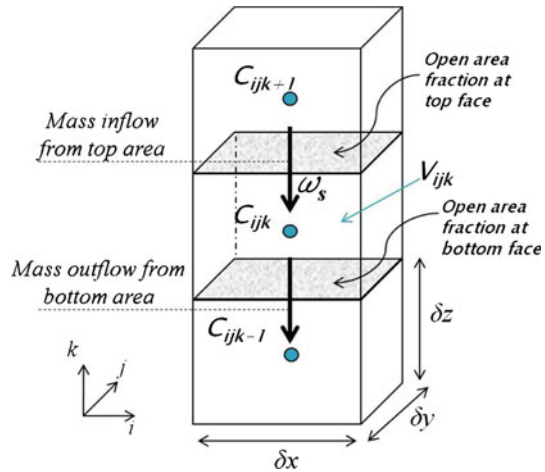
$$\omega_s = \frac{g d_s^2}{18\nu} \left(\frac{\rho_s - \rho_w(T)}{\rho_w(T)} \right), \tag{17}$$

where $\rho_w(T)$ is the water density defined as a function of temperature from Gill [15]. The temporal evolution of the particle field can then be treated in an Eulerian manner using a turbulent advection-diffusion equation. Thus, Eq. (3) becomes:

$$\frac{\partial \phi}{\partial t} + \frac{\partial}{\partial x_i}(u_i \phi) = \frac{\partial}{\partial x_i} \left(\Gamma \frac{\partial \phi}{\partial x_i} - \overline{u_i' \phi'} \right) + \frac{\partial}{\partial z}(\omega_s \phi). \tag{18}$$

In the computational cell (i, j, k), final density ρ_{ijk}^n at time level n is calculated as a function of temperature and particle concentration as follows:

$$\rho_{ijk}^n = \rho_w(T)_{ijk}^n \left[1 + (G-1) \frac{V_{s_{ijk}}^n}{V_{ijk}} \right], \tag{19}$$

where $\rho_w(T)_{ijk}^n$ is the water density in cell (i, j, k) at temperature T^oC; $V_{s_{ijk}}^n$ is the particles volume in cell (i, j, k), which is updated each time step due to deposition of particles as shown in Fig. 4; V_{ijk} is the total fluid volume in cell (i, j, k); and G is the specific gravity of a particle.

We assumed that the forces induced by particle settling have a negligible influence on the motion of the fluid phase. Thus, the motion of the fluid phase is solved using the Navier-Stokes equation without two-way coupling between the particles and the fluid. However, in order to describe the motion induced by particle-driven buoyant forces, the turbulent advection-diffusion equation is coupled with the Navier-Stokes equation through the buoyancy term. Since we are only interested in mixture flows with small mass loadings, the Boussinesq approximation in which the density variations affects only the gravitational term can be invoked in the Navier-Stokes equation.

3 Problem configuration and simulation cases

In order to use the experimental data for the validation of the numerical model, simulations are performed under conditions that correspond to the laboratory experimental setup in

Sutherland et al. [39] and Gladstone et al. [16]. The first series of simulation cases are performed to identify the propagation dynamics of IGC. The simulation results of the first series of simulations are compared with the experimental measurements of Sutherland et al. [39]. The second series of simulations are performed to numerically reproduce the experiments of Gladstone et al. [16] so as to evaluate the capability of the numerical model to capture the important aspects of PDGC. Brief description of these series of simulations are provided next.

3.1 Intrusive gravity currents in a two-layer fluid (IGC)

The model simulation setup is configured to be identical to the experimental dimensions in Sutherlands experiments (i.e. 197.1 cm long by 17.6 cm wide by 48.5 cm height). The lock-length (l) behind the gate is fixed at 18.6 cm and the total water depth (H) is set equal to 20 cm. We selected a total of three simulation cases from the experimental setup [39]. For defining the different simulation cases, we used the dimensionless parameters ϵ, σ, and Δ, respectively. In two of the simulation cases (Cases 1 and 2), the density of the lock fluid is equal to the depth-weighted average of the upper and lower layers ($\epsilon = 0$, symmetrical condition). In the first case, the depth of the two layers in the ambient fluids is also equal ($h_o = h_1$) with $\sigma = 0.02$. In the second case, the depth of the two layers in the ambient fluids is not equal ($h_o \neq h_1$) with $\sigma = 0.02$. The third simulation (Case 3) is conducted with $\epsilon \neq 0$ (asymmetrical condition). Table 1 shows the initial conditions for all the simulations.

The computational domain for the IGC simulations is illustrated in Fig. 5 with the specified boundary conditions. The computational grid size in the x-, z-directions is chosen to be 1.0 mm for laterally-averaged simulations. For 3-D simulations, the computational grid is extended in lateral (y) direction. However, due to computational constraints, a coarser grid

Table 1 Summary of IGC simulation setup

Case #	Case name	ϵ	Δ	H (cm)	h_o	h_1	$\bar{\rho}$ (kg/m^3)	ρ_1	ρ_o	ρ_d
1	IGC	0	0	20	10	10	1,010	1,020	1,000	1,010
2	IGC	0	0.75	20	17.5	2.5	1,002.5	1,020	1,000	1,002.5
3	IGC	0.625	0.75	20	17.5	2.5	1,002.5	1,020	1,000	1,015

The nondimensional parameters are defined as $\epsilon = (\rho_d - \bar{\rho})/(\rho_1 - \rho_o)$, $\Delta = (h_o - h_1)/H$ where $\bar{\rho} = (\rho_o h_o + \rho_1 h_1)/H$
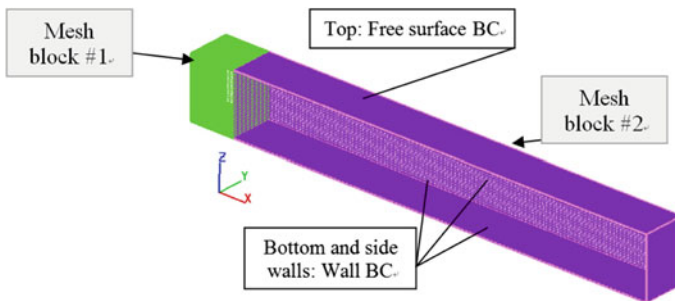
Fig. 5 Computational domain depicting the mesh and the boundary conditions for the simulations corresponding to the experimental setup of Sutherland et al. [39]

Table 2 Initial conditions for the IGC simulation cases

Case no.	Mesh block	#1		Mesh block	#2		
	T (°C)	SS (mg/l)	ρ_d (kg/m³)	T (°C)	SS (upper/lower)	ρ_o/ρ_1	h_o/h_1 (cm/cm)
1	4	16,100	1,010	4	0/32160	1,000/1,020	10/10
2	4	4,050	1,002.5	4	0/32160	1,000/1,020	17.5/2.5
3	4	24,110	1,015	4	0/32160	1,000/1,020	17.5/2.5

size is used in the lateral direction (i.e. $\Delta x = \Delta z = 1.0$ mm and $\Delta y = 30$ mm), with a computational grid comprising of approximately 2.5 million cells. The domain is divided into two sub-domains using multi-block meshes.

The first mesh block is created in the fluid area filled behind lock gate and the second mesh block contains the larger sub-domain that contains a receiving fluid (a two-layer fluid).

The wall boundary is specified as non-tangential stress areas with a no-slip condition. At the walls, k and ϵ are computed using a logarithmic law of wall function [33], and given by

$$k = \frac{u_*^2}{\sqrt{C_\mu}}, \ \epsilon = \frac{u_*^3}{\kappa y_o}, \tag{20}$$

where u_* = shear velocity; κ = von Kármán constant; and y_o = the normal distance from the boundary wall to the location of tangential velocity. At the free surface, no flux conditions are imposed. For initial conditions in the numerical simulations, the velocity is set to zero and the density difference for each simulation is developed by adjusting temperature (T) and adding concentration (suspended sediments concentration SS). The initial conditions for temperature and concentration for the IGC simulation cases are shown in Table 2.

3.2 Particle-driven gravity currents (PDGC)

The computational domain and setup used in this study correspond to the laboratory experimental setup of Gladstone et al. [16] (i.e. 5.7 m long, 0.2 m wide, and 0.4m water depth). They carried out a series of experiments using mixtures containing two different diameters of silicon carbide particle (25 μm and 69 μm). The silicon carbide particles ($\rho_s = 3,217$ kg/m³) were used to create the excess density in the experiments. The concentration of particle suspension was set to be 11.2 kg/m³. Reduced gravitational acceleration (g') was calculated to be 0.076 m/s². We performed a total of 4 simulations (case 4 through 7) to validate the numerical results with the the experiments of Gladstone et al. [16] as shown in Table 3. Note, in cases 4 and 7, only one particle size is used for the simulations, while sediment mixtures comprising two particle sizes are used for the others. Furthermore, additional simulations with different particle sizes were performed to investigate the dynamics of PDGC and determine the conditions under which particles settle out of gravity currents.

4 Results and discussion

In this section, we first provide results from IGC simulation cases (cases 1 through 3, shown in Table 1). Numerical simulations exhibit changes in IGC dynamics in response to changes in ϵ and Δ. We also provide physical validation of the numerical model through quantitative comparisons with analytical solutions and experimental measurements. We then use PDGC

Table 3 PDGC simulation cases using mixtures comprising of different particle diameters

Case no.	Case name	T (°C)	SS (kg/m^3)	ρ_d (kg/m^3)	d_s#1 (69 μm)	d_s#2 (25 μm)	ρ_a (kg/m^3)
4	PDGC	20	11.2	1,005.9	0 %	100 %	998.2
5	PDGC	20	11.2	1,005.9	50 %	50 %	998.2
6	PDGC	20	11.2	1,005.9	80 %	20 %	998.2
7	PDGC	20	11.2	1,005.9	100 %	0 %	998.2

simulations to explore the fate and transport of suspended particles in the flow. Finally, we present flow regimes, which can vary subject to changes in particle sizes.

4.1 Intrusive gravity currents (IGC, case 1 through 3)

In the first symmetrical case (case 1: $\epsilon = 0$ and $\Delta = 0$), the simulation snapshots are created to visualize the temporal evolutions of the intrusive gravity current. The simulation snapshots are compared with images taken from the laboratory experiments of Sutherland et al. [39] (see Fig. 6).

The temporal and spatial distributions of concentration are solved using scalar transport equations. The transported concentration contributes to changes in the density in each of the computational cells. The molecular diffusivity is neglected and only turbulent diffusivity is used to account for turbulent mixing effect.

Figure 6 shows that the fluid contained behind the lock gate collapses symmetrically and propagates along the interface after the lock gate is removed. The head already starts to form and is visible after 2 s. The initial collapse begins with rapid acceleration and the current head becomes uniform in shape after 26 s. As it propagates to the right end of the wall, the head of the gravity current causes strong mixing, resulting in mass loss and dilution in the head. The temporal evolution of the gravity current is illustrated well with images taken from both the experiments and the numerical simulations as shown in Fig. 6. It is clear that the numerical model with RNG k–ϵ and LES approaches predict well the dynamics of IGC developed with perfect symmetrical conditions ($\epsilon = 0$ and $\Delta = 0$). It is also evident that the LES resolves the fine scales associated with the mixing that occurs in the vicinity of the gravity current head. The formation of Kelvin–Helmholtz billows showing vertical structure behind the head of IGC is reproduced very well by LES closure scheme, but this detail is not captured by the RANS simulation using the RNG k–ϵ closure scheme. The numerical results of RNG k–ϵ shows the front shape and body of the gravity current without Kelvin–Helmholtz billows. In the 3-D high resolution simulations of gravity currents, the formation of lobe and cleft at the head of gravity current was generally observed in both experimental and computed density currents [27,29,30]. In this study, 3-D LES closure scheme also shows reasonable agreement with the laboratory experiment, but the lobe and cleft at the head was not evident due to the coarser grid size that was used in the lateral (y) direction.

The traveling distance calculated from both RNG k–ϵ and LES runs are plotted as a function of time in Fig. 7. It shows very good agreement with experimental measurements and the analytical solutions from Sutherland et al. [39], Lowe et al. [26], and Benjamin [3]. In order to identify the difference between laterally-averaged and 3-D simulations, we additionally consider the 3-D simulation results in Fig. 6. It is clear that there is no significant difference between the 2-D and 3-D LES simulation results.
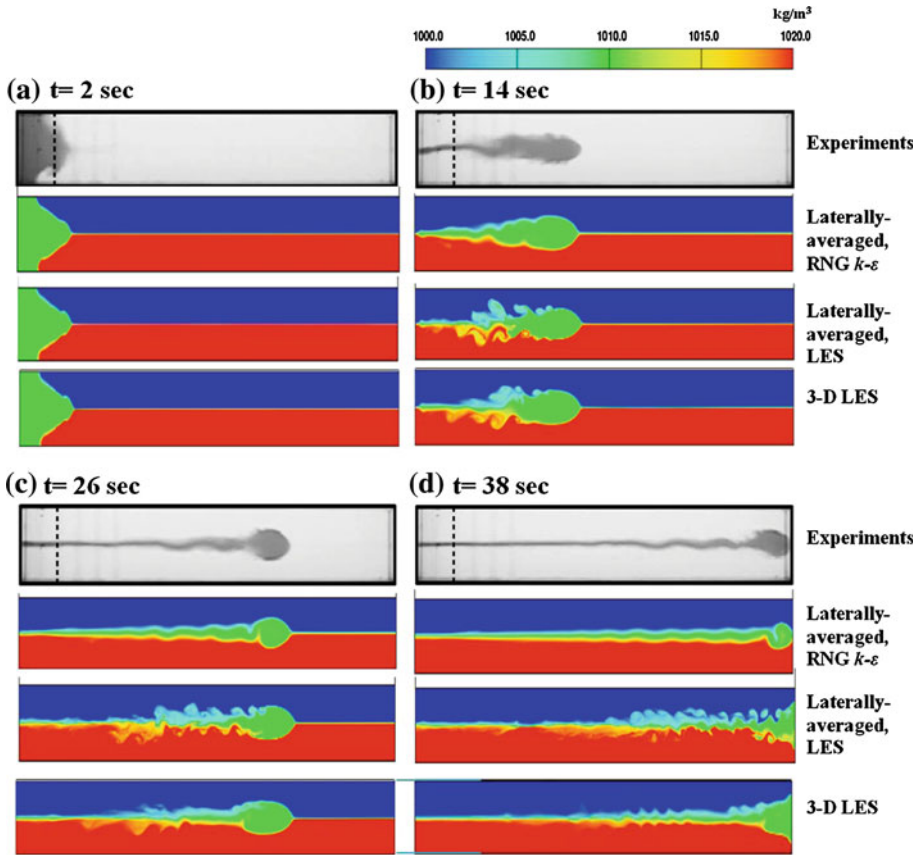
Fig. 6 Temporal evolutions of an intrusive gravity current (*IGC*) for case 1 (symmetrical case) where experimental results of Sutherland et al. [39] were visualized by adding dye. Density contours showing temporal evolutions in laterally-averaged and 3-D numerical simulations were calculated based on RNG k–ϵ and LES. The $x - z$ cross-sections were taken along the center line in the y-direction
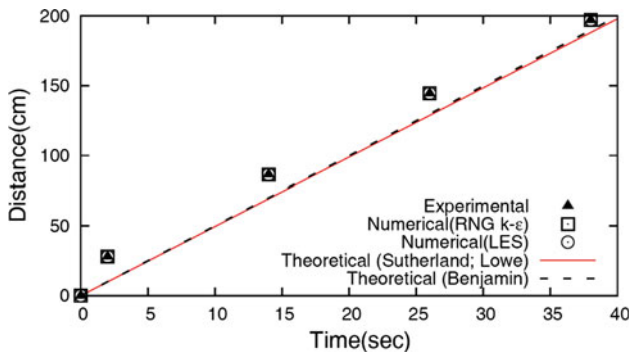

Fig. 7 Traveling distance of IGC as a function of time for case 1. The *square* and *circle symbols* indicate simulation results from this study while *triangles* indicate experimental results from Sutherland et al. [39]. The *solid line* indicates the analytical solution from Sutherland et al. [39] and Lowe et al. [26]. The *dashed line* indicates the analytical solution from Benjamin [3] ($U_d/\sqrt{g\sigma H} \simeq 0.252$ with $h_d/H \simeq 0.23$ where the h_d was taken from the 3-D LES simulation result captured at 26 s)
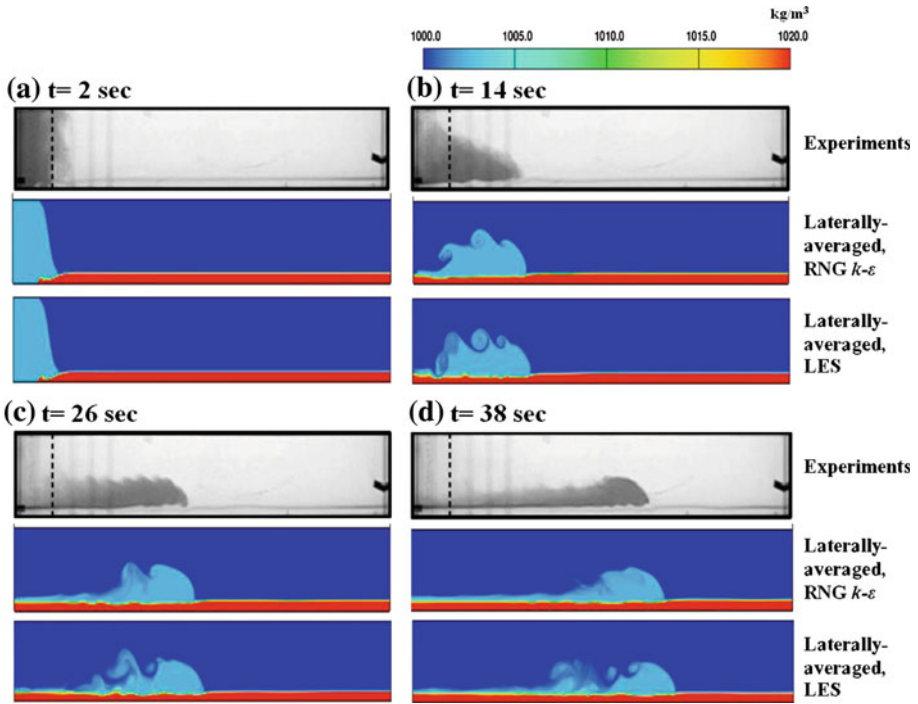
Fig. 8 Temporal evolutions of the intrusive gravity current (*IGC*) for case 2 (symmetrical case) where experimental results of Sutherland et al. [39] were visualized by adding dye. Density contours showing temporal evolutions in laterally-averaged simulations were calculated based on RNG k–ϵ and LES models

In the second symmetrical case (case 2: $\epsilon = 0$ and $\Delta \neq 0$), we observe different dynamics compared to the perfect symmetrical case (case 1) as shown in Fig. 8 In this case, the propagation speed is observed to be slower than that of the gravity current in case 1. In particular, the gravity current does not form a symmetrical head as it propagates. This is because the return flows in the upper layer and lower layer of the ambient fluid move at different speeds and they interact with the end wall differently. Sutherland et al. [39] also mentioned that the density difference between lock and ambient upper-layer fluid is small. Therefore the top return flow takes longer to be established, resulting in mixing between the lock and ambient fluid behind lock-gate, whereas the return flow in the lower layer of the ambient fluid intrudes into the lock fluid rapidly with weak vorticity. After the collapse phase, the lock fluid forms the head and tail of the gravity current. Shear instability occurs only across the interface between the gravity current and the upper layer. The shape of the gravity current seems similar to a gravity current propagating over a no-slip, bottom (BBGC).

By comparing the experiment with the simulation at $t = 14$ s (see Fig. 8b), the numerical simulation shows less mixing than the experiment where some initial mixing is introduced by vorticity in the upper lighter layer behind lock gate. After the collapse phase, the numerical simulations also show weaker shear instabilities in the rear part of the tail region (Fig. 8c). Sutherland et al. [39] note that the mixing between lock fluid and the upper-later ambient fluid is promoted by the vorticity created by the gate removal. In the numerical simulations, the vorticity developed by the lock-gate removal cannot be simulated. However, the propagation speed of the intrusive current is still correctly reproduced by the numerical simulations.
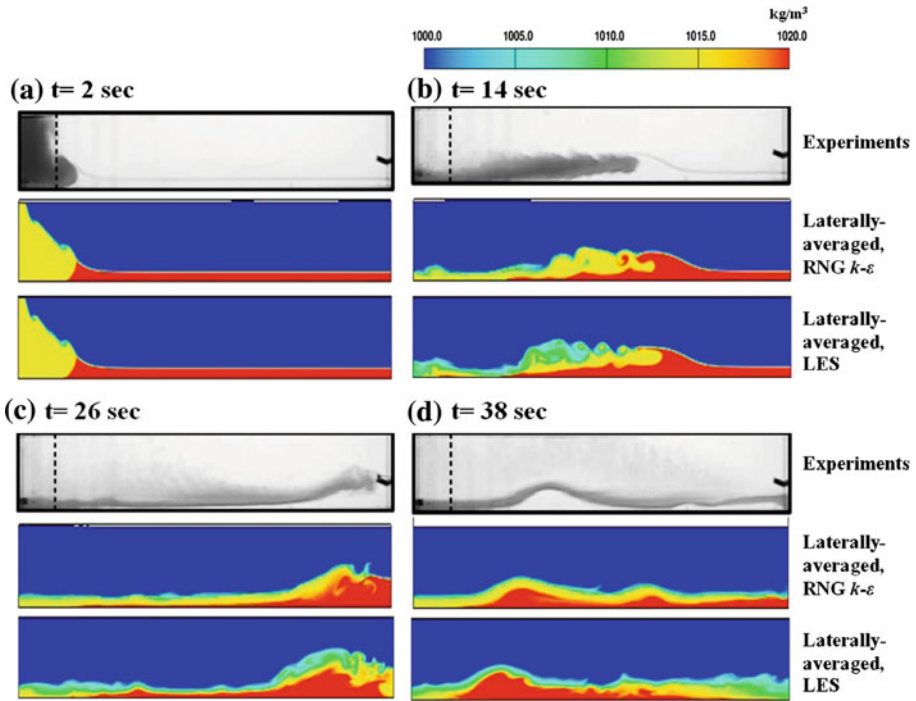
Fig. 9 Temporal evolutions of the intrusive gravity current (IGC) for case 3 (asymmetrical case) where experimental results of Sutherland et al. [39] were visualized by adding dye. Density contours showing temporal evolutions in laterally-averaged simulations were calculated based on RNG k–ϵ and LES models

In simulations with symmetrical conditions (cases 1 and 2), the amplitude of the waves is small enough to keep the sharp and stable interface ahead of the intrusive gravity current (not deflected vertically). Similar observations in laboratory experiments have been reported by Sutherland et al. [39] and Cheong et al. [6]. They conclude that the interfacial wave is probably negligible for the dynamics of the intrusion propagating into a two-layer fluid with symmetrical conditions. However, a large amplitude internal wave, as is apparent from the images in Fig. 9, is observed in the simulations with asymmetrical condition (case 3, $\epsilon \neq 0$ and $\Delta \neq 0$). Figure 9 shows that the internal wave propagates faster than the gravity current. In this situation, it is not easy to determine analytical solutions for propagation speeds because the process of developing waves including reflected waves strongly affects the dynamics of the gravity current.

The propagation speed of IGC is one of the important parameters investigated through lock-exchange flow experiments. We plot propagation distances at different instants in time from both numerical simulations and the experiments, as shown in Fig. 10. We assess the forecasting performance of the numerical model using absolute mean error (AME) and root mean square error ($RMSE$), as defined by:

$$AME = \frac{1}{n}\left(\sum_{i=1}^{n} |M_i - S_i|\right),$$ (21)

Fig. 10 Quantitative evaluation of IGC simulation errors using AME and RMSE. The *dots* indicate the propagation distances of IGC (Case 1, Case 2, Case 3 shown in Table 2) at each measurement time ($t = 2$, 14, 26, and 38 s)
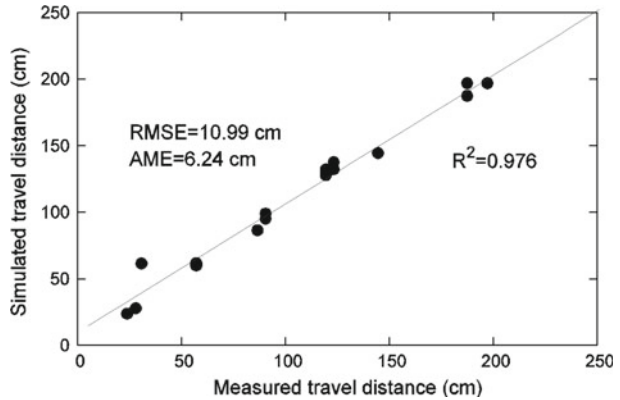
$$RMSE = \sqrt{\frac{1}{n} \sum_{i=1}^{n} (M_i - S_i)^2}, \qquad (22)$$

where n is number of data points, M_i are the laboratory measurements, and S_i are the simulation results. The AME and RMSE for propagation distances of IGC at each measurement time (t= 2, 14, 26, and 38 s) are calculated to be 6.24 and 10.99 cm, which are less than less than 6 % of the total propagation distance of 200 cm., based on the data shown in Fig. 10. Also shown in Fig. 10 is the coefficient of determination, R^2 which provides a measure of the goodness of fit of the simulation results. Overall, the numerical model shows good quantitative agreement for predicting propagation speed and temporal-spatial evolutions of IGC.

4.2 Particle-driven gravity currents (PDGC, cases 4 through 7)

The temporal evolutions of PDGC are captured for each simulation at $t = 0$, 5, 15, 25, 30, and 50 s with concentration contour after the release of the particle added fluid (see Figs. 11, 12). During the initial collapse, the propagating gravity currents show similar evolutions and almost constant velocity for all simulation runs. However, as they travel further, the gravity currents in each simulation run show different speeds depending on the particle sizes in the mixture.

In Fig. 13, we compare the simulated and observed current front position versus time. The numerical model successfully captures the decreasing propagation speed due to the different deposition rates between each particle size. The curve shows constant slope during the slumping phase of gravity currents. In this flow regime, the velocity of the currents remains constant regardless of the proportion of the coarse and fine particles. Thereafter, propagation speed decreases as the particle size increases. We observe that the divergence between experiments and numerical results increases with time. A possible reason for the observed divergence between laboratory experiments and numerical results might be due to the difficulty in modeling the particle resuspension mechanism from bottom sediments. In the present numerical model, particles reaching to the bottom can not be resuspended. Therefore the celerity calculations in the model are expected to be slightly lower than the laboratory measurement.

The transported concentration by the gravity current is plotted as a function of particle size at $t = 100$ s (see Fig. 14). The ratio of transported concentration C_o at $t = 100$ s to
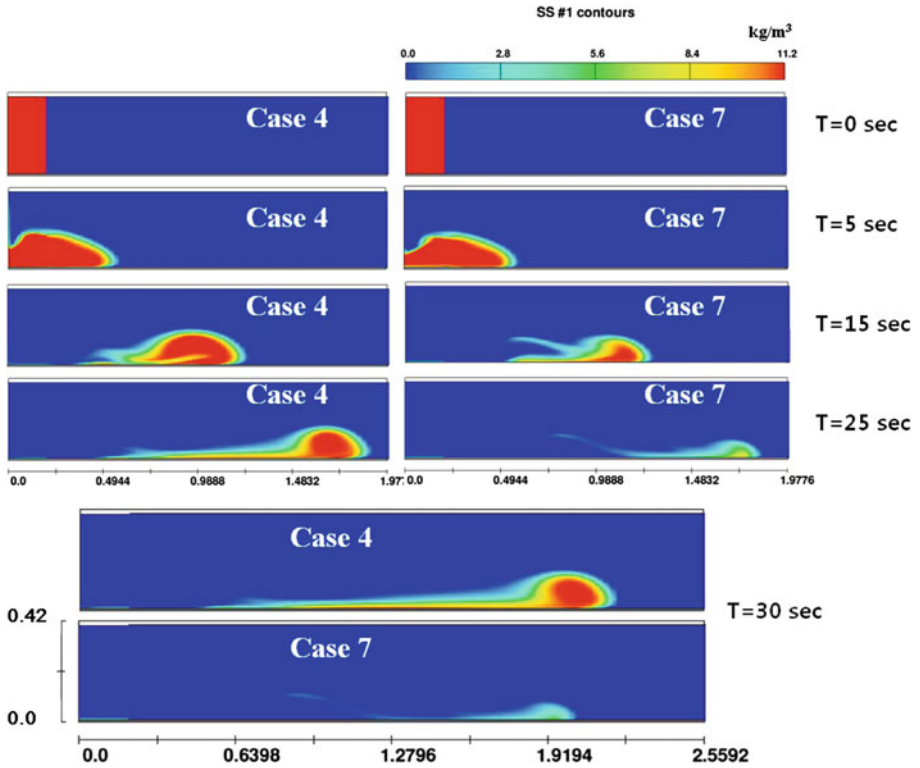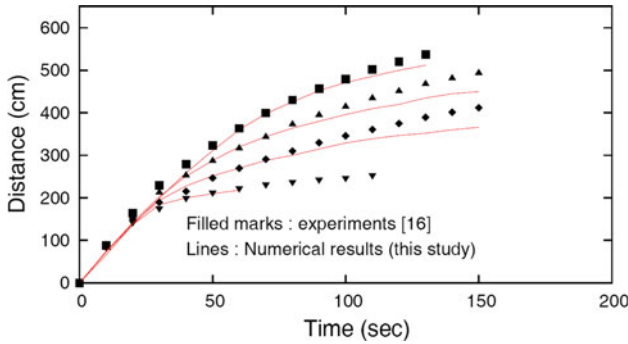
Fig. 11 Simulated temporal evolutions of PDGC, plotted with concentration shaded contours for simulation case 4 and case 7, based on the laterally-averaged RANS method with RNG k–ϵ
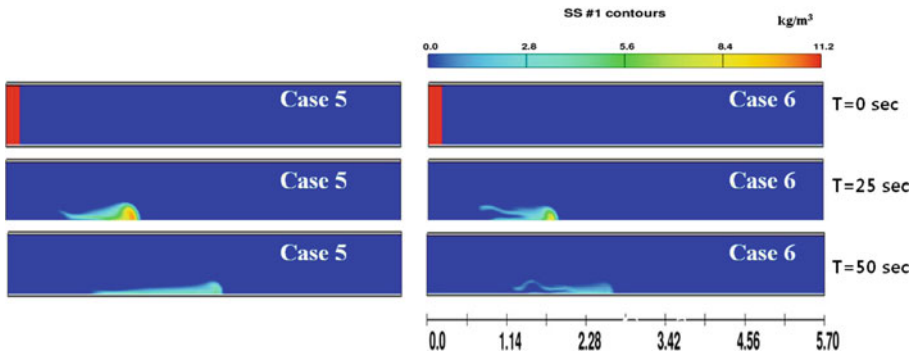

Fig. 12 Simulated temporal evolutions of PDGC, plotted with concentration shaded contours for simulation cases 5 and 6, based on the laterally-averaged RANS method

initial concentration C_i of the gravity current varies as a function of the particle diameter d_s. The flow patterns of PDGC can be subdivided into three regimes describing the effect of particle size. The effect of particle settling velocity on the propagation speed of the PDGC is negligible at a value of d_s less than about 16 μm. The different deposition rates depending

Fig. 13 Simulated temporal evolutions of PDGC, for cases 4, 5, 6, and 7, based on RANS method with RNG k–ϵ. The *filled marks* indicate the percentage of coarse (69 μm) and fine (25 μm) size fractions by mass from experiments [16]. The *black square* indicates 100 %, 25 μm; The *black triangle* indicates 50 %, 25 μm and 50 %, 69 μm; The *black lozenge* is 20 %, 25 μm and 80 %, 69 μm; The *black downward triangle* indicates 100 %, 69 μm
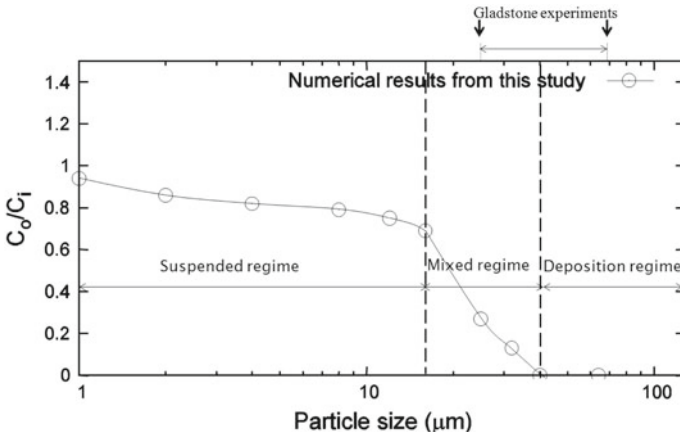
Fig. 14 The transported concentration by PDGC as a function of particle size at $t = 100$ s. C_i is initial concentration of the fluid inside the lock. C_o is the concentration horizontally transported at $t = 100$ s by PDGC

on d_s, however, significantly contribute to the dynamics when $16\,\mu m < d_s < 40\,\mu m$. When $d_s > 40\,\mu m$, the PDGC rapidly loses its forward momentum.

5 Conclusions

This study simulated the propagation dynamics of gravity currents using a three-dimensional, non-hydrostatic numerical model. Two different turbulence closure schemes (RNG k–ϵ and LES) were employed, and their comparative performance was presented. The numerical simulations focus on two different types of density flows (IGC and PDGC). In the study of IGC, the evolution profile and propagation speed were compared with laboratory experiments and analytical solutions. The numerical model shows good quantitative agreement for predicting temporal, and spatial evolutions of IGC. In particular, the simulated propagation speed is in

excellent agreement with experimental measurements for simulation case 1. The evaluation of the numerical model for predicting the propagation speed of IGC was presented using AME and RMSE which were calculated to be 6.24 and 10.99 cm, respectively. These values are less than 6 % of the total propagation distance of 200 cm. The simulation results do not show any considerable discrepancies between RNG k–ϵ RANS and LES techniques. The results clearly demonstrate the viability of the RNG k–ϵ closure scheme within a RANS framework for field scale applications with fast computational times without significant loss in performance. Field scale simulations are simply not feasible with LES or DNS because such techniques are computationally intensive and thus become prohibitive for field applications.

In the study of PDGC, the FLOW-3D model successfully captured the decreasing propagation speed due to the different deposition rates which vary with particle size. The transported concentration by the gravity current was plotted as a function of particle size at $t = 100$ s. The ratio C_i/C_o of transported to initial concentration of the gravity current varies as a function of the particle diameter d_s. Particle transport by gravity currents can be classified into three regimes: (1) a suspended regime (d_s is less than about 16 μm) where the effect of particle deposition rate on the propagation dynamics of gravity currents is negligible i.e. such flows behave like homogeneous fluids (IGC); (2) a mixed regime (16 μm $< d_s <$ 40 μm) where deposition rates significantly change the flow dynamics; and (3) a deposition regime ($d_s >$ 40 μm) where the PDGC will rapidly lose forward momentum due to fast deposition rates. We note that these flow regimes are valid for particles with specific gravity of 3.22 settling in water. Extension of this study that include a pick-up function for the resuspension of particles is ongoing to investigate erodability of bottom beds by gravity currents.

References

1. Altinakar MS, Graf WH, Hopfinger EJ (1990) Weakly depositing turbidity current on a small slope. J Hydraul Res 28(1):55–80
2. An SD (2011) Interflow dynamics and three-dimensional modeling of turbid density currents in Imha Reservoir, South Korea. Ph.D. dissertation in Department of Civil and Environmental Engineering, Colorado State University
3. Benjamin TB (1968) Gravity currents and related phenomena. J Fluid Mech 31:209–248
4. Britter RE, Simpson JE (1981) A note on the structure of the head of an intrusive gravity current. J Fluid Mech 112:459–466
5. Cantero MI, Balachandar S, García MH (2008) An Eulerian-Eulerian model for gravity currents driven by inertial particles. Int J Multiphase Flow 34:484–501
6. Cheong HB, Kuenen JJ, Linden PF (2006) The front speed of intrusive gravity currents. J Fluid Mech 552:1–11
7. Choi SU, García MH (2002) k–ϵ turbulence modeling of density currents developing two dimensionally on a slope. J Hydraul Eng ASCE 128(1):55–63
8. Chung SW, Gu R (1998) Two-dimensional simulations of contaminant currents in stratified reservoir. J Hydraul Eng ASCE 124(7):704–711
9. De Cesare G, Schleiss A, Hermann F (2001) Impact of turbidity currents on reservoir sedimentation. J Hydraul Eng ASCE 127(1):6–16
10. De Cesare G, Boillat G, Schleiss A (2006) Circulation in stratified lake due to flood-induced turbidity currents. J Environ Eng ASCE 132(11):1508–1517
11. Faust KM, Plate EJ (1984) Experimental investigation of intrusive gravity currents entering stably stratified fluids. J Hydraul Res 22:315–325
12. FLOW-3D release 9.3 (2007) User guide and manual. Flow Science Inc, Santa Fe
13. Fringer OB, Gerritsen MG, Street RL (2006) An unstructured-grid, finite-volume, nonhydrostatic, parallel coastal ocean simulator. Ocean Modell 14:139–173
14. Georgoulas A, Angelidis B, Panagiotidis T, Kotsovinos N (2010) 3D numerical modelling of turbidity currents. J Environ Fluid Mech 10:603–635
15. Gill AE (1982) Atmosphere-ocean dynamics. Philosophical transactions. Series A, Mathematical, physical, and engineering sciences. Academic Press, New York

16. Gladstone C, Phillips JC, Sparks RSJ (1998) Experiments on bidisperse, constant-volume gravity currents: propagation and sediment deposition. Sedimentology 45(5):833–843
17. Hallworth MA, Huppert HE (1998) Abrupt transitions in high-concentration, particle-driven gravity currents. Phys Fluids 10(5):1083–1087
18. Härtel C, Meiburg E, Necker F (2000) Analysis and direct numerical simulation of the flow at a gravity-current head, Part I, Flow topology and front speed for slip and no-slip boundaries. J Fluid Mech 418:189–212
19. Heimsund S (2007) Numerical simulation of turbidity currents: a new perspective for small- and large scale sedimentological experiments. Master thesis in Sedimentology/Petroleum Geology Department of Earth Science University of Bergen
20. Hirt CW (1993) Volume-fraction techniques: powerful tools for wind engineering. J Wind Eng Ind Aerodyn 46&47:327–338
21. Hirt CW, Nichols BD (1981) Volume of fluid (VOF) method for the dynamics of free boundaries. J Comput Phys 39:1–11
22. Holyer JY, Huppert HE (1980) Gravity currents entering a two-layer fluid. J Fluid Mech 100(04):739–767
23. Huppert HE (2006) Gravity currents: a personal perspective. J Fluid Mech 554:299–322
24. Keulegan GH (1957) Thirteenth progress report on model laws for density currents an experimental study of the motion of saline water from locks into fresh water channels. U.S. Natl Bur Standards Rept 5168
25. Lesieur M, Metais O, Comte P (2005) Large-eddy simulations of turbulence. Cambridge University Press, Cambridge
26. Lowe RJ, Linden PF, Rottman JW (2002) A laboratory study of the velocity structure in an intrusive gravity current. J Fluid Mech 456:33–48
27. McCaffrey WD, ChouxCM Baas JH, Haughton P (2003) Spatio-temporal evolution of velocity structure, concentration and grain size stratification within experimental particulate gravity currents. Mar Petrol Geol 20:851–860
28. Middleton GV (1966) Experiments on density and turbidity currents: I. Motion of the head. Can J Earth Sci NRC Research Press 3(5):627–637
29. Necker F., Hartel C., Kleiser L., Meiburg E. (2002) High-resolution simulations of particle-driven gravity currents. Int J Multiphase Flow 28:279–300
30. Ooi SK, Constantinescu G, Weber L (2007) A numerical study of intrusive compositional gravity currents. Phys Fluids 19:076602. doi:10.1063/1.2750672
31. Parker G, Fukushima Y, Pantin HM (1986) Self accelerating turbidity currents. J Fluid Mech 171:145–181
32. Pope SB (2000) Turbulent flows. Cambridge University Press, Cambridge
33. Rodi W (1980) Turbulence models and their application in hydraulics-A state of the art review. Int Assoc Hydraul Res Public, 2nd edn. Balkema
34. Rooij F, Linden PF, Dalziel SB (1999) Saline and particle-driven interfacial intrusions. J Fluid Mech 389:303–334
35. Schmitt FG (2007) About Boussiness turbulent viscosity hypothesis: historical remarks and a direct evaluation of its validity. Comptes Rendus Mécanique 335(9&10):617–627
36. Shin JO, Dalziel SB, Linden PF (2004) Gravity currents produced by lock exchange. J Fluid Mech 521:1–34
37. Simpson JE (1987) Gravity currents: in the environment and the laboratory. Cambridge University Press, Cambridge
38. Smagorinsky J (1963) General circulation experiments with the primitive equations. Mon Wea Rev 91:99–164
39. Sutherland BR, Kyba PJ, Flynn MR (2004) Intrusive gravity currents in two-layer fluids. J Fluid Mech 514:327–353
40. Turner JS (1979) Buoyancy effects in fluids. Cambridge University Press, Cambridge
41. Ungarish M (2009) An introduction to gravity currents and intrusions. CRC Press, Boca Raton
42. Ungarish M, Huppert HE (2004) On gravity currents propagating at the base of a stratified ambient: effects of geometrical constraints and rotation. J Fluid Mech 521:69–104
43. Von Kármán T (1940) The engineer grapples with nonlinear problems. Bull Am Math Soc 46(8):615–684
44. Yakhot V, Orszag SA (1986) Renormalization group analysis of turbulence. I. Basic theory. J Sci Comput 1(1):3–51